

Improving the predictive power of empirical shell-model Hamiltonians

J. A. Purcell,¹ B. A. Brown,¹ B. C. He,² S. R. Stroberg,² and W. B. Walters³

¹*Department of Physics and Astronomy, Michigan State University,
East Lansing, Michigan 48824-1321, USA and Facility for Rare Isotope Beams,
Michigan State University, East Lansing, Michigan 48824-1321, USA*

²*Department of Physics and Astronomy, University of Notre Dame, Notre Dame, IN 46556 USA*

³*Department of Chemistry and Biochemistry, University of Maryland, College Park, Maryland 20742, USA*

(Dated: December 16, 2024)

We present two developments which enhance the predictive power of empirical shell model Hamiltonians for cases in which calibration data is sparse. A recent improvement in the ab initio derivation of effective Hamiltonians leads to a much better starting point for the optimization procedure. In addition, we introduce a protocol to avoid over-fitting, enabling a more reliable extrapolation beyond available data. These developments will enable more robust predictions for exotic isotopes produced at rare isotope beam facilities and in astrophysical environments.

The nuclear shell model is a ubiquitous framework for interpreting nuclear structure data. In particular, the interacting shell model, or configuration interaction (CI) approach quantitatively reproduces and explains a vast amount of spectroscopic data. These CI calculations require the specification of an effective Hamiltonian. While ab initio methods have made great progress recently in deriving these Hamiltonians from the underlying inter-nucleon interactions, they have not yet achieved the precision obtained with phenomenological Hamiltonians adjusted to data. The gold standard for the phenomenological CI paradigm is the USD family of Hamiltonians, which reproduce spectra with a root-mean-squared deviation of better than 200 keV. In this relatively small model space, the vast amount of available data is more than sufficient to constrain the parameters of the Hamiltonian. In contrast, many of the nuclei that will be studied in the coming decades at rare isotope facilities, including the majority of nuclei relevant for r -process nucleosynthesis, will live in larger model spaces where data is sparse. This enhances the importance of maximizing predictive power with minimal data. In addition, the information content of various experimental data is often redundant, in terms of which parameters are constrained; in order to reliably extrapolate beyond the available data it is critical to avoid over-fitting. In this Letter, we (1) demonstrate that an improved ab initio calculation provides a starting point which requires fewer phenomenological adjustments, and (2) utilize a training/testing partitioning scheme to avoid over-fitting.

Microscopic configuration-interaction (CI) calculations for specific regions of nuclei are based on a description in terms of a selected set of shell-model orbitals (the model space) with a Hamiltonian operator

$$H = E_0 + \sum_{\alpha} \epsilon_{\alpha} \hat{n}_{\alpha} + \sum_{\alpha < \beta, \gamma < \delta} \sum_J V_J(\alpha\beta; \gamma\delta) \hat{T}_J(\alpha\beta; \delta\gamma) \quad (1)$$

that is represented by the energy of the closed core E_0 , single-particle energies (SPE) ϵ_{α} , and two-body matrix

elements (TBME) $V_{JT}(\alpha\beta; \gamma\delta)$: In principle, three-body matrix elements could be included, but they dramatically increase the complexity of the problem, and their main effect is to modify the SPE and TBME, so they are generally not treated explicitly. The SPE and TBME can be obtained from a realistic NN (possibly with 3N) interaction, renormalized to the valence space in some way, for example using many-body perturbation theory [1], shell model coupled cluster [2], or the valence-space in-medium similarity renormalization group (VS-IMSRG) [3]. We use the latter approach in this work, including the effects of 3N interactions via the normal-ordered two-body (NO2B) approximation. This leads to values for E_0 , ϵ and V_J which are nucleus-dependent [3].

A commonly applied approximation when optimizing empirical Hamiltonians is to use a nucleus-independent set of SPE and TBME. The TBME may include some smooth mass dependence, e.g. $A^{-0.3}$ [4–8]. Within this approximation the SPE and TBME can be used parameters to achieve an improved description of measured binding energies and excitation energies (energy data) with the goal of obtaining improved wavefunctions and improved predictions for new energy data and for other observables.

The singular-value decomposition (SVD) method provides a systematic approach for finding the most important linear combinations of the N_p SPE and TBME parameters which can be determined by the data [5, 9, 10]. One starts with wavefunctions obtained from a Hamiltonian derived from the best available ab-initio input. With these wavefunctions, the expectation value of the Hamiltonian provides a linear combination of SPE and TBME for each of the N_d energy data. The SVD amounts to a diagonalization of the $N_p \times N_p$ fit matrix solution to χ^2 minimization, and provides singular values and associated eigenvectors (linear combinations of SPE and TBME). The largest singular values are associated with the most well determined linear combinations, and smallest singular values are associated with the least well determined combinations. The TBME associated with these least

well determined combinations will have some influence on the extrapolations to new energy data and to the calculations of other observables. One must choose a singular value cut-off N_c . Below the cut off one can use TBME obtained from the best available ab-initio input. This provides a new set of SPE and TBME that can be used to obtain an improved set of wavefunctions. One iterates the SVD fits and the wavefunction calculations until convergence.

Examples of Hamiltonians obtained in this way with protons and neutrons are, USDA/B [4] and USDC/I [5] for the $\{0d_{5/2}, 0d_{3/2}, 1s_{1/2}\}$ (*sd*) model space, GPFX1A [6] for the $\{0f_{7/2}, 0f_{5/2}, 1p_{3/2}, 1p_{1/2}\}$ (*fp*) model space, and JUN45 [7] and jj44b (Appendix A of [8]) for the $\{0f_{5/2}, 1p_{3/2}, 1p_{1/2}, 0g_{9/2}\}$ (*jj44*) model space. For all of these Hamiltonians the root-mean-square-deviation (RMSD) between the calculated and experimental energy data is 150-200 keV. This is to be compared with the results of ab-initio type calculations over the same regions of nuclei where the RMSD is much larger (see Fig. 9 of [3] for the *sd* model space). In all of these cases, there is abundant experimental data to constrain the fitted Hamiltonian across the entire model space. However, for very exotic nuclei relevant for rare isotope beam facilities and *r*-process nucleosynthesis, the data will be sparse and strongly biased toward the most stable region of the model space. In such cases, it is possible to overfit to the available data, yielding an Hamiltonians that extrapolates poorly to more exotic nuclei.

In this Letter, we demonstrate that by using an improved ab-initio starting point and by reserving some data for validation, we can improve the predictive power of the resulting Hamiltonian when extrapolating beyond the fit data. For our application, we consider data for low-lying states for all nuclei between ^{78}Ni and ^{100}Sn that can be described by protons in $\{0f_{5/2}, 1p_{3/2}, 1p_{1/2}, 0g_{9/2}\}$ (the $\pi j4$ model space), which requires 4 SPE and 65 TBME with $T = 1$ associated with the valence protons. This space has been considered previously with SVD derived Hamiltonians [7], [11], [12] as well as those obtained VS-IMSRG methods [13]. The data we employ consists of 22 ground-state binding energies and 167 excitation energies. The region between ^{90}Zr and ^{100}Sn is well established territory where many wavefunctions are dominated by $\{1p_{1/2}, 0g_{9/2}\}$ configurations that requires only nine TBME that can be established directly from the energy data [14], [15], [16], [17], [18], [19], [20]. There is new data for nuclei close to ^{78}Ni whose structure is dominated by the $\{0f_{5/2}, 1p_{3/2}, 1p_{1/2}\}$ subset of orbitals. Importantly, many of the single-particle energies for these orbitals associated with low-lying states in ^{79}Cu [21] and ^{99}In [22] are now established. The results from the IMSRG methods discussed below are also shown. In the supplementary material we review the experimental data for nuclei between ^{78}Ni and ^{86}Kr . This includes a discussion of intruder states that can be attributed to orbital

configurations that are not part of the $\pi j4$ model space. These intruder states are excluded from the data set used for the SVD fits.

As a starting point for our fitting procedure, we use Hamiltonians derived with the VS-IMSRG. These are obtained using the EM 1.8/2.0 NN+3N interaction [24] in a harmonic oscillator basis with frequency $\hbar\omega = 12$ MeV, truncated to 13 major shells ($2n + l \leq e_{\text{max}} = 12$). We normal order with respect to the Hartree-Fock ground state of the reference and discard the residual 3N interaction. We then decouple the $\pi j4$ valence space, using the Magnus formulation of the IMSRG. The results labeled IMSRG(2) are obtained with the standard approximation [3], truncating all operators at the two-body level throughout the flow, including inside nested commutators. The results labeled IMSRG(3f2) include the recently introduced correction in which intermediate three-body operators arising in nested commutators are incorporated by rewriting the double commutator in a factorized form while maintaining the same computational scaling as the IMSRG(2) approximation[25]. As in ref. [25], we include factorized terms with a one-body intermediate during the flow, and include terms with a two-body intermediate at the end of the flow. We perform the procedure for two different references, ^{78}Ni and ^{100}Sn , corresponding to empty and full valence spaces, respectively, and take the average of the two resulting valence space Hamiltonians as our starting point for the fitting procedure.

Intuitively, the more realistic the ab initio Hamiltonian is, the less it needs to be modified to produce results that are in agreement with experiment. Shown in FIG. 2 is a comparison of the TBME obtained with the IMSRG(2) and IMSRG(3f2) approximations, indicating the magnitude of the uncertainty due to the many-body truncation. These uncertainties propagate into our effective Hamiltonians, and ultimately the resulting wavefunctions and calculations made with them. The main difference is that the $J = 0$, $T = 1$ TBME are about 30 percent weaker for IMSRG(3f2) compared to those from IMSRG(2).

FIG. 1 shows the RMSD for the two different IMSRG starting points as a function of the number of VLC. The resulting Hamiltonians will be labeled by $pn-ia$ where n indicates the number of VLC, and a indicates the ab-initio starting Hamiltonian, $a = 2$ for IMSRG(2) and $a = 3$ for IMSRG(3f2). The purple line shows the energy-RMSD between the calculated and experimental energy data. Both starting points approach a similar level of energy-RMSD as the number of VLC increase. The major difference between the approach to this threshold is shown by the red points, which shows the RMSD between the fitted and ab-initio TBME. For IMSRG(2) the TBME-RMSD goes above the 200 keV level with 6 VLC, while for the results for IMSRG(3f2) do not reach this level until around 55 VLC. It can also be seen that the energy-RMSD for the fitted data set falls substantially

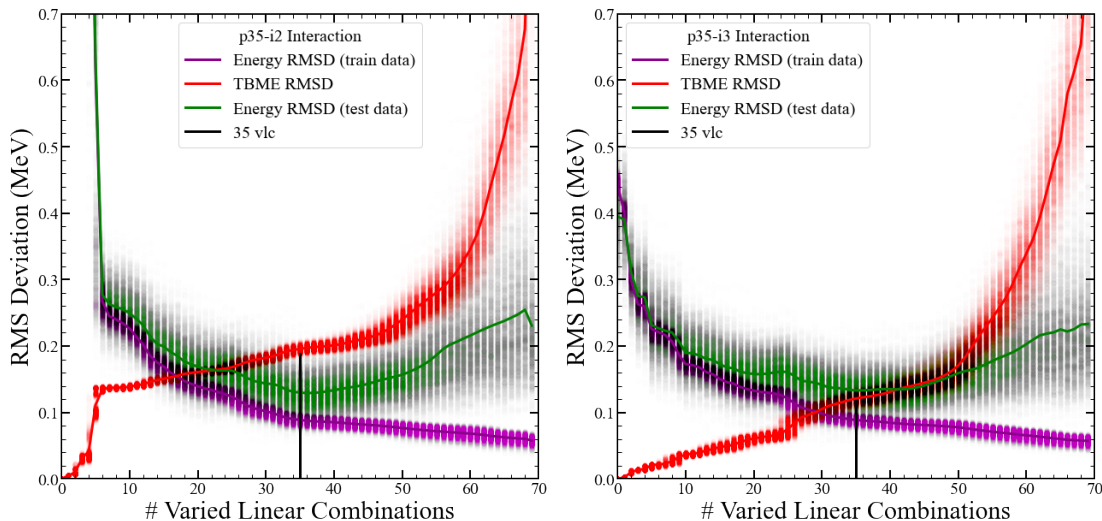


FIG. 1. The purple points show the energy-RMSD between theory and experiment as a function of the number of VLC, and the red points show the TBME-RMSD between the IMSRG and fitted Hamiltonians. The lines are the results for the pn-i2 and pn-i3 Hamiltonians. We also show points for the 2000 batches of randomly sampled experimental training data discussed in the text, purple points for the training energy data set, and green points for the predicted data set.

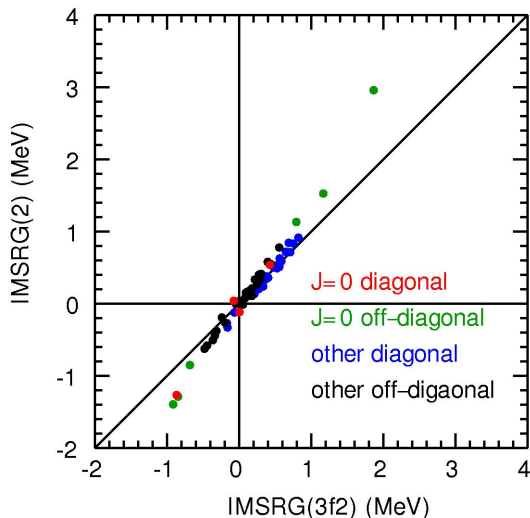


FIG. 2. Comparison of the TBME obtained with the two versions of the IMSRG method - the y-axis involves the 2-body truncation and the x-axis involves the factorized approximation. The TBME are colored according to the type of overlap that they describe.

after only one VLC for IMSRG(3f2), while IMSRG(2) requires nearly 15 VLC to reach the same level of accuracy. These results highlight the improvement made for the TBME by the IMSRG(3f2) method. The deviations for each state in the fitted energy data obtained with the p1-i3 and p35-i3 Hamiltonians are shown in FIG. 3.

An essential purpose of these effective Hamiltonians is to achieve some level of predictive power; this is high-

lighted in FIG. 1. To obtain the scatter of the points around the central fit values as well as the green points in this figure, all of the known experimental data for this model space was randomly partitioned into training (80%) and testing (20%) batches. The training batch was used to vary the parameters of our Hamiltonian, and the testing set was used in the calculation of RMSD - in this way our fitted Hamiltonian is predicting the results of data that it had not seen in the fitting procedure. The sampling process was repeated 2000 times to generate a distribution of calculations for each VLC, and for each set of Hamiltonian parameters. The green curve highlights the predictive capacity of each Hamiltonian as the number of VLC's is increased. It can be seen that each Hamiltonian approaches an energy-RMSD minimum (a maximum for the predictive power) at about 35 VLC. In fact the RMSD is reasonably small over the range of 15-35 VLC. This is significant because it indicates that we can achieve some benchmark level of predictive power with fewer modifications to our starting Hamiltonian with the factorization method given by [25]. This becomes critically significant when one considers effective Hamiltonians for larger model spaces where producing these effective Hamiltonians and using them to make predictions becomes computationally intensive, or where data is sparse or redundant in terms of constrained parameters.

The calculations presented in FIG. 5 sampled from the full range of data $28 \leq Z \leq 50$, so the predictions are in some sense an interpolation. It is of great interest to also understand the robustness of extrapolations beyond the fit data. To do this, we partition the data so that the training data only contains $Z > 36$, and consider

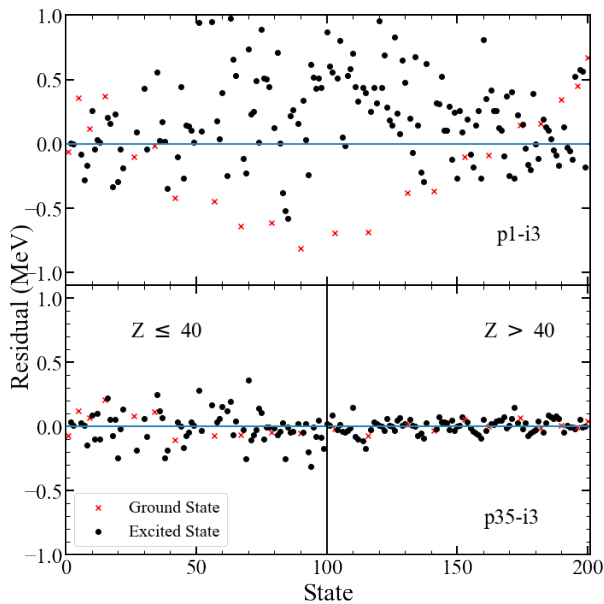


FIG. 3. Residual between states calculated from effective Hamiltonian with both (a) 1 VLC and (b) 35 VLC, and corresponding experimental states used to generate the effective Hamiltonian. Both effective Hamiltonians are obtained from the IMSRG(3f2) starting point. We note that the p35-i3 energy differences are larger below $Z = 90$ (120 keV) compared those above that (50 keV). The main reason is that the higher-mass data is dominated by only nine TBME associated with the $\{1p_{1/2}, 0g_{9/2}\}$ orbitals, whereas the lower mass data is dominated by 30 TBME associated with the $\{0f_{5/2}, 1p_{3/2}, 1p_{1/2}\}$ orbitals. The supplementary material includes a listing of the experimental and p35-i3 fitted energy data as well as a listing of the p35-i3 SPE and TBME.

the RMSD for $Z \leq 36$. We find that the RMSD in the neutron-rich validation set decreases as the number of VLC is increased, up to 35, where we obtain an RMS of approximately 300 keV. Beyond 35 VLC, the RMSD grows again, indicating that we have begun to over-fit, and extrapolative power deteriorates.

In conclusion, we found that two markedly different starting Hamiltonians can be tuned to produce quite similar results when a robust dataset and fitting method are implemented. The degree to which these starting Hamiltonians must be modified intuitively depends on how successful the initial parameters are at reproducing the known experimental data. The goal is to produce wavefunctions that are realistic and predictive. We conclusively find that the factorized approximation of IMSRG(3f2) given by [25] produces a starting Hamiltonian that requires less modification to reproduce experimental data than ab initio Hamiltonians produced by other methods, meaning that this Hamiltonian is inherently more realistic - a result illustrated clearly in FIG. 1 and FIG. 4. The TBME-RMSD is much smaller with the recently introduced VS-IMSRG(3f2) corrections involving

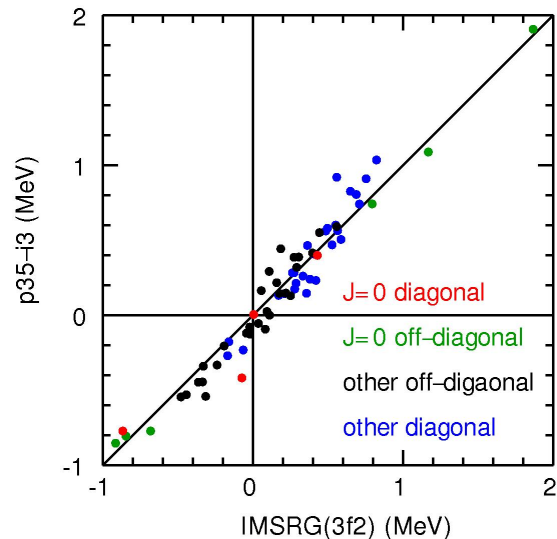


FIG. 4. Comparison of the IMSRG(3f2) and p35-i3 TBME.

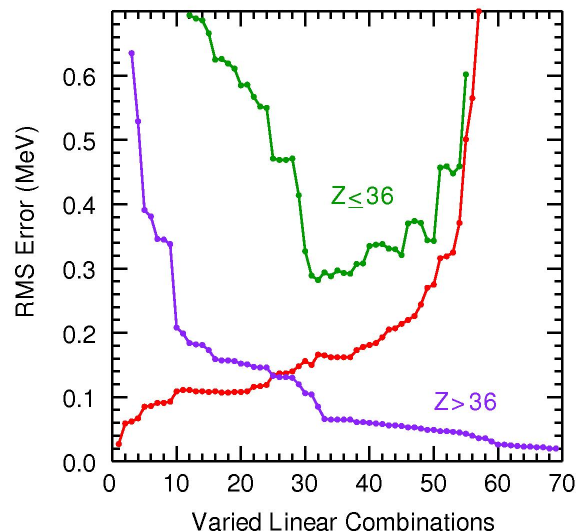


FIG. 5. Results obtained when the fitted data set is restricted to $A > 86$. See caption to FIG. 1

three-body operators. Thus, 3f2 should provide a better input for the linear combinations of parameters that cannot be determined from VLC fits to energy data. In addition, we have demonstrated that utilizing the RMSD from the training/validation partitioning in the fit procedure helps protect against over-fitting, and yields more robust extrapolation to data beyond that used in the fit.

We acknowledge support from NSF grants PHY-2110365, and PHY-2340834.

SUPPLEMENTARY MATERIAL

Initial Procedure: χ^2 Minimization

Our starting Hamiltonian has a set of parameters $\vec{p}^s = (p_1^s, \dots, p_{N_p}^s)$. This Hamiltonian defines a starting set of eigenvectors $|\phi_k^s\rangle$ that can be used to calculate the operator overlaps β_i^k so that each associated eigenvalue λ_k can be calculated in equation (1). Then we seek to minimize the ℓ^2 -norm of the residual ($\vec{\chi}$) between the N_d measured experimental energies and calculated energy eigenvalues:

$$\min_{\vec{p} \in \mathbb{R}^{N_p}} \chi^2 = \min_{\vec{p} \in \mathbb{R}^{N_p}} \sum_{k=1}^{N_d} \left(\frac{E_k^{exp} - \lambda_k(\vec{p})}{\sigma_k} \right)^2$$

where $\sigma_k^2 = (\sigma_k^{exp})^2 + (\sigma_k^{th})^2$. We can reorganize the fitting by expanding λ_k and defining the expected energy contribution from $H^1(\vec{p})$ to be $\epsilon_k^{exp} = E_k^{exp} - E_k^0$. Now our χ^2 minimization looks like:

$$\min_{\vec{p} \in \mathbb{R}^{N_p}} \chi^2 = \min_{\vec{p} \in \mathbb{R}^{N_p}} \sum_{k=1}^{N_d} \left(\frac{\epsilon_k^{exp} - \epsilon_k(\vec{p})}{\sigma_k} \right)^2$$

We simplify the notation further first by re-expressing our data components $z_k^{exp} = \epsilon_k^{exp}/\sigma_k$ and then considering the model components:

$$z_k(\vec{p}) = \frac{\epsilon_k(\vec{p})}{\sigma_k} = \sum_{i=1}^{N_p} p_i \frac{\beta_i^k}{\sigma_k}$$

We can arrange the components of the experimental data into a data vector $\vec{z}^{exp} = [z_1^{exp}, \dots, z_{N_d}^{exp}]^T$, and similarly for the model components we can represent a model vector through matrix-vector multiplication:

$$\begin{bmatrix} z_1(\vec{p}) \\ \vdots \\ z_{N_d}(\vec{p}) \end{bmatrix} = \begin{bmatrix} \beta_1^1/\sigma_1 & \cdots & \beta_{N_p}^1/\sigma_1 \\ \vdots & \ddots & \vdots \\ \beta_1^{N_d}/\sigma_{N_d} & \cdots & \beta_{N_p}^{N_d}/\sigma_{N_d} \end{bmatrix} \begin{bmatrix} p_1 \\ \vdots \\ p_{N_p} \end{bmatrix}$$

If we recognize that $\frac{\beta_j^k}{\sigma_k} = \frac{\partial z_k(\vec{p})}{\partial p_j}$ then the matrix above must by definition be the transposed Jacobian (J^T) of the vector-valued function $\vec{z}(\vec{p}) = [z_1(\vec{p}), \dots, z_{N_d}(\vec{p})]^T$. This allows us to re-express our χ^2 minimization as:

$$\min_{\vec{p} \in \mathbb{R}^{N_p}} \chi^2 = \min_{\vec{p} \in \mathbb{R}^{N_p}} \|\vec{z}^{exp} - J^T \vec{p}\|^2$$

Minimizing this with respect to each parameter p_j gives N_p equations of the form:

$$\begin{aligned} \frac{\partial \chi^2}{\partial p_j} &= 2 \sum_{k=1}^{N_d} \left(\frac{\epsilon_k^{exp} - \epsilon_k(\vec{p})}{\sigma_k} \right) \left(-\frac{1}{\sigma_k} \frac{\partial \epsilon_k(\vec{p})}{\partial p_j} \right) \\ &= -2 \sum_{k=1}^{N_d} \left(\frac{\epsilon_k^{exp} \beta_j^k}{\sigma_k^2} - \sum_{i=1}^{N_p} p_i \frac{\beta_i^k \beta_j^k}{\sigma_k^2} \right) = 0 \end{aligned}$$

which leaves us with the condition that:

$$\sum_{k=1}^{N_d} \frac{\epsilon_k^{exp} \beta_j^k}{\sigma_k^2} = \sum_{k=1}^{N_d} \sum_{i=1}^{N_p} p_i \frac{\beta_i^k \beta_j^k}{\sigma_k^2}$$

Notice that If we now define the quantities:

$$e_j = \sum_{k=1}^{N_d} \frac{E_k^{exp} \beta_j^k}{(\sigma^k)^2} \quad \text{and} \quad G = \begin{bmatrix} \gamma_{11} & \cdots & \gamma_{1p} \\ \vdots & \ddots & \vdots \\ \gamma_{p1} & \cdots & \gamma_{pp} \end{bmatrix}$$

where

$$\gamma_{ij} = \sum_{k=1}^{N_d} \frac{\beta_i^k \beta_j^k}{(\sigma^k)^2} = \sum_{k=1}^{N_d} \frac{\beta_j^k \beta_i^k}{(\sigma^k)^2} = \gamma_{ji} \in \mathbb{R} \quad (G = G^T)$$

we can rewrite the N_p equations as a single vector equation:

$$\vec{e} - G\vec{x} = 0 \quad \longrightarrow \quad \vec{x} = G^{-1}\vec{e} \quad (2)$$

Since the G -matrix is real and symmetric, it is diagonalizable. The step of solving for \vec{x} shown in equation (2) is only possible if G is invertible, meaning that none of the eigenvalues of the G -matrix are 0. This process can be used to find a new \vec{x} that can be used to calculate new eigenvalues for the new eigenstates $|\phi_k'\rangle$, repeating until convergence.

Note: G^{-1} is referred to as the error matrix because its diagonal entries are the square of parameter errors and the off-diagonals are related to correlations between parameters.

SVD Procedure

The Hamiltonian parameters are often highly correlated, and the fit can be re-expressed in terms of an orthonormal basis of uncorrelated SVD parameters. Since G is real and symmetric, its SVD is identical to an eigen-decomposition - the SVD for G and G^{-1} are:

$$G = ADA^T \quad \text{and} \quad G^{-1} = AD^{-1}A^T$$

where:

- $D \in \mathbb{R}^{p \times p}$ is a matrix of diagonal positive elements $D_{ii} > 0$.
- $A \in \mathbb{R}^{p \times p}$ is a rotation matrix whose columns form an orthonormal basis of our SVD parameter space.
- D^{-1} is a diagonal matrix whose elements are inverses of the elements of D - i.e. $[D^{-1}]_{ii} = d_i = \frac{1}{D_{ii}}$

With these substitutions in the result of our minimization we have:

$$\vec{x} = AD^{-1}A^T\vec{e} \quad \longrightarrow \quad A^T\vec{x} = D^{-1}A^T\vec{e}$$

Now we express the rotations of \vec{x} and \vec{e}

$$\vec{y} = A^T\vec{x} \quad \text{and} \quad \vec{c} = A^T\vec{e}$$

resulting in

$$\vec{y} = D^{-1}\vec{c} \quad \longrightarrow \quad y_i = d_i c_i \quad (3)$$

Here the uncorrelated SVD parameters y_i are expressed as a linear combination of the Hamiltonian parameters x_i with associated errors d_i - explicitly:

$$\vec{y} = A^T\vec{x} = \sum_{l=1}^p x_l \vec{a}_l^T \quad \longrightarrow \quad y_i = \sum_{l=1}^p x_l [A^T]_{il} \quad (4)$$

where \vec{a}_l^T is the l 'th column of A^T . When d_i is large the SVD parameters y_i experience a large change from a correspondingly small change in the data c_i , meaning that the corresponding linear combination of Hamiltonian parameters y_i is poorly determined by the given data set. We can establish a cutoff criterion on what is poorly determined linear combination of Hamiltonian parameters y_i based on the magnitude of the corresponding d_i

Fitting Algorithm

1. Starting from the best available Hamiltonian parameters \vec{x}^s we construct and diagonalize the G -matrix to obtain D_{ii} eigenvalues and the orthonormal basis for our parameter space.
2. Mutually independent SVD parameters y_i are determined in the fit from equation (4). Explicitly:

$$y_i = d_i c_i = d_i \sum_{l=1}^p e_l [A^T]_{il}$$

Simultaneously, linear combinations of ab initio Hamiltonian parameters are determined from equation (5). Explicitly:

$$\vec{y}^* = A^T\vec{x}^* \quad \longrightarrow \quad y_i^* = \sum_{l=1}^p x_l^* [A^T]_{il}$$

3. One defines a cutoff criterion δ , and updated linear combinations \vec{y}^a are defined by only adopting well-determined values y_i with respect to this cutoff, and leaving ab initio values y_i^* for the rest:

$$y_i^a = \begin{cases} y_i & (d_i \leq \delta) \\ y_i^* & (d_i > \delta) \end{cases}$$

The number of well-determined linear combinations is N_d

4. With the updated set of model parameters \vec{y}^a one recovers the Hamiltonian parameters by inverting the rotation:

$$\vec{x}^a = (A^T)^{-1}\vec{y}^a$$

5. This set of Hamiltonian parameters takes the place of \vec{x}^s as input to the first step of this algorithm, and is used to obtain the next set of parameters \vec{x}^b . This process is repeated until convergence.

Experimental data for the N = 50 isotones

The structure of ^{78}Ni has been studied via knock-out reactions and shows a group of excited states between 2.6 and 4.0 MeV [26]. Levels with spins and parities of 2^+ and 4^+ are suggested at 2.60 and 3.18 MeV, respectively. The relatively high excitation of these states indicates that the wavefunction of ^{78}Ni is dominated by closed-shell configuration of $Z = 28$ for protons and $N = 50$ for neutrons. For protons, a $0f_{7/2}$ proton can be moved across the $Z = 28$ proton gap into the $0f_{5/2}$ and $1p_{3/2}$ orbitals leading to a multiplet of states with J^π ranging from 1^+ to 6^+ . For neutrons, a $0g_{9/2}$ neutron can be moved across the $N = 50$ shell gap into the $0d_{5/2}$ orbital, leading to a multiplet of states from 2^+ to 7^+ . Also for neutrons, a $1p_{1/2}$ neutron can be moved across $N = 50$ into the $0d_{5/2}$ orbital, leading to states with 2^- and 3^- .

The level structure of ^{79}Cu has also been studied in knock-out reactions [21]. Two low-lying levels are proposed at 0.656 and 1.511 MeV with the gamma-decay sequence of 1.511 MeV to 0.656 MeV to the ground state. These experimental energies are compared to shell-model predictions in FIG. 6. All of these predictions give an ordering of $1/2^-$, $3/2^-$ and $5/2^-$ corresponding to single-particle configurations of $1p_{1/2}$, $1p_{3/2}$ and $0f_{5/2}$, respectively.

The ^{79}Cu ground-state spin-parity is not measured. The lighter Cu isotopes are measured to have ^{71}Cu ($J = 3/2$), ^{73}Cu ($J = 3/2$), ^{75}Cu ($J = 5/2$) and ^{77}Cu ($J = 5/2$) [28]. Shell-model calculations give negative-parity ground states. The energy differences between the lowest levels with $J = 3/2^-$ and $J = 5/2^-$ obtained with the JUN45 Hamiltonian [7] in the $jj44$ model space are shown in Fig. (6). They are compared with experiment for $^{69,71,73,75}\text{Cu}$ using the energies of the states that are suggested to have $J = 3/2$ and $5/2$ [28]. For ^{79}Cu we give the experimental results assuming a ground state and first excited states with J^π of $5/2^-$ and $3/2^-$, respectively, (solid black line) and $3/2^-$ and $5/2^-$, respectively, (dashed black line). The systematics of these energy differences compared to theory are consistent with the ground state of ^{79}Cu having $J^\pi=5/2^-$, with the first excited state at 0.656 MeV having $J^\pi=3/2^-$. When compared to the shell-model calculations in Fig. (1), the

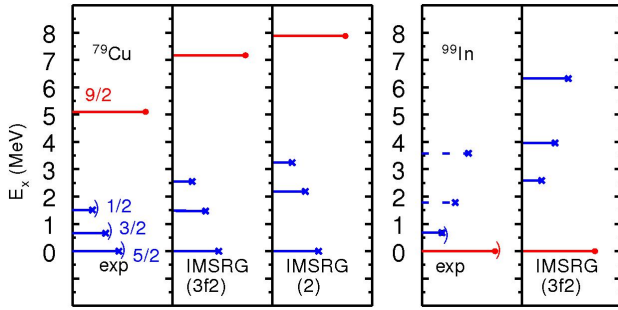


FIG. 6. Levels in ^{79}Cu and ^{99}In . The J value is correlated with the horizontal length of the lines: blue for negative parity and red for positive parity. Experimental levels with suggested J^π assignments are indicated by ”)” [21, 22]. The $9/2^+$ energy shown in the experimental panel was obtained from our $p35-i3$ Hamiltonian. The dashed blue lines for ^{99}In show excitation energies based on the observations in ^{131}In [23]. In the $\pi j4$ model space, the states for ^{79}Cu are interpreted as single-particle states relative to a ^{78}Ni closed shell, and states for ^{99}In are interpreted as single-hole states relative to a ^{100}Sn closed shell. The IMSRG results are based on calculations for ^{78}Ni and ^{100}Sn .

second-excited state at 1.511 MeV is expected to have $J^\pi=1/2^-$. The sequence of gamma decays observed in [21] is consistent with the $(1/2^-, 3/2^-, 5/2^-)$ sequence. In the single-particle model this gives a $1p_{1/2} - 1p_{3/2}$ spin-orbit splitting of 0.855 MeV. This smaller the value of 1.66 MeV shown by the MCSM calculations in FIG. 2 of [21]. The experimental $1/2^- - 3/2^-$ splitting in ^{131}In is suggested to be 988 keV [27].

Other excited states in ^{79}Cu are observed starting at 2.9 MeV. It is natural to understand these as intruder coming from the knockout of an $0f_{7/2}$ proton in ^{80}Zn leading to $2p - 1h$ states in ^{79}Cu . Three transitions at 2.94, 3.88, and 4.30 MeV of about equal intensity that decay directly to the ground state and could represent fragments of the $0f_{7/2}$ hole strength.

The first excited 2^+ level in ^{80}Zn was identified in a Coulomb excitation study at 1.492 MeV [29]. The Coulex experiment obtains $B(E2, \uparrow)=20.1(16) e^2 \cdot \text{fm}^4$. Further level structure has been provided from knock-out reactions where a 4_1^+ level is placed at 1.979 MeV [30]. In [30] three other levels are identified at 2.627, 2.820 and 3.174 MeV. The latter two decay only to the 4_1^+ level. The experimental energies are compared to those from the JUN45 [7] and MCSM [31] Hamiltonians in FIG. 4 of [30]. With only two protons in the $0f_{5/2}$ and $1p_{3/2}$ orbitals beyond ^{78}Ni , the maximum positive-parity spin is 4^+ . Lifetimes and $B(E2)$ values have been determined for both the 2^+ and 4^+ levels [32].

Level structure for ^{81}Ga has come from extensive study of the beta decay of the $5/2^+$ ground state of ^{81}Zn , as well as by both multi-nucleon transfer (MNT) and knock-

out reactions. A recent decay scheme was obtained using laser-ionized ^{81}Zn and has provided the most detail [33]. The ground-state $5/2^-$ assignment is supported by laser hyperfine methods [34]. Two excited $3/2^-$ levels are identified, along with one clear $9/2^-$ level and one clear $11/2^-$ level [35]. $11/2^-$ is the highest spin that can be obtained by three protons in the $0f_{5/2}$ and $1p_{3/2}$ orbitals. Levels proposed at higher spins would have to involve either the $0g_{9/2}$ proton orbital, or intruder states coming from the neutron excitations across the $N = 50$ shell gap. A possible higher-spin level has been reported by both [35] and [37] at 2.766 MeV that decays to the $11/2^-$ level. Ref. [35] also reports on the gamma decay from a level at 3.093 MeV to the 2.766 MeV level, that could have even higher spin. Transitions at 770 keV and 990 keV were observed in (p,2p) reactions that feed into the $11/2^-$ level at 1.952 MeV [36].

The basic level structure for ^{82}Ge has been provided by beta-decay of the 2^- ground state of ^{82}Ga [38], [39], and beta-delayed neutron decay of the $5/2^-$ ground-state of ^{83}Ga . Also by Coulomb excitation, MNT studies [40], [41], [42], [43], and fission-product gamma-ray studies [44]. Triple coincidences between gamma rays (in MeV) at 1.348 (2^+), 0.938 (4^+), and 0.940 (6^+) establish the yrast sequence. As 6^+ is the highest possible spin for four protons in the $0f_{5/2}$ and $1p_{3/2}$ levels, this level would have to arise from some cross-shell excitation, or involvement of the $0g_{9/2}$ proton orbital. A proposed 7^+ level at 3.948 MeV has been reported [45] that decays to the 6^+ level at 3.228 MeV. These $5^+, 6^+, 7^+$ states are understood as coming from the excitation of a neutron in the $0g_{9/2}$ orbital into the $1d_{5/2}$ orbital across the $N = 50$ shell gap [45, 46]. These high-spin particle-hole configurations are also observed in ^{84}Se , ^{86}Kr and ^{88}Sr [45] at increasingly higher excitation energy.

The 2_2^+ MeV level is placed at 2.216 MeV by strong population in all of the decay studies as well as the presence of a 2.216 MeV ground-state transition. The 0_2^+ level at 2.333 MeV is similarly observed in decay studies with no ground-state transition. Two levels at 2.702 and 2.714 MeV are observed in all of the decay studies, but not observed in the MNT and fission-gamma studies are possible 3^+ and 1^+ levels, respectively. Two levels at 2.883 and 2.933 MeV are observed in decay, MNT, and fission studies that decay only to the two lower-energy 4_1^+ and 4_2^+ levels and are candidates for 4^+ and 5^+ assignments. The $B(E2)$ value for the 1.348 MeV level has been measured by [47].

The level structure of ^{83}As with 33 protons has the most complex structure among the odd-proton $N = 50$ isotones. It has 5 valence protons and is exactly half way from $Z = 28$ to $Z = 38$. The maximum spin available by breaking both pair of protons that occupy the $0f_{5/2}$ and $1p_{3/2}$ orbitals would be $13/2^-$. Extensive data exist for the structure of ^{83}As from decay and MNT reaction studies. With 5 protons, the Fermi level has moved up in

energy to the point that a $9/2^+$ state associated with the $0g_{9/2}$ proton state should be observed. However, firm identification has remained elusive. A candidate is present at 2.777 MeV that has been assigned ($9/2^+$). [48]. However, in other studies, no level was assigned as $9/2^+$ [49], [50], [51]. The gamma decay data clearly show low-energy levels that have should have proton configurations, then a gap around 3 MeV where the neutron particle-hole states should be present [52]. As in ^{81}Ga , three excited levels in ^{83}As at 0.307, 1.544, and 1.867 MeV are clearly identified as $3/2^-$, $9/2^-$, and $11/2^-$, respectively.

Extensive data are also present for the structure of ^{84}Se . Not only from beta decay and multi-nucleon transfer (MNT) studies, but also from the $^{82}\text{Se}(t,p)^{84}\text{Se}$ 2-neutron transfer reaction. and where cross-shell neutron states are possible, the level density rises rapidly. Levels populated in beta decay were reported by Hoff et. al. [53]. High-spin structures have been reported by several groups [42], [50].

Three prominent higher-spin levels have been observed at 3.372 [6^+], 3.639 [5^+], and 3.704 [6^+] MeV with the spin and parity assignments derived from Coulex data [54], [55], [56]. A proposed 7^+ level has been identified in several papers at 4.407 MeV. Unlike ^{82}Ge , it is possible to obtain spin and parity of 7^+ by aligning all six protons in the $0f_{5/2}$, $1p_{3/2}$, and $1p_{1/2}$ orbitals [45]. Two 0^+ levels below 3 MeV are identified in both reports at 2.247 and 2.655 keV. Gamma-ray transitions from both of these levels are seen by cross-correlations in the Carpenter data set [42]. Three other 0^+ levels are proposed at 1.967, 2.716, and 2.740 MeV for which no gamma transitions are observed.

The level structure of ^{85}Br is quite important for these studies as the data for the spins and parities are on a far firmer basis. Polarized proton pickup in the $^{86}\text{Kr}(d,^3\text{He})^{85}\text{Br}$ reaction provide definitive data for the locations of the $3/2^-$, $5/2^-$ and $1/2^-$ states at 0, 0.345, and 1.191 MeV, respectively. These are associated with $1p_{3/2}$, $0f_{5/2}$, and $1p_{1/2}$ single proton hole states Angular distribution data for the high-spin levels also provide a definite location of the $9/2^+$ level at 1.859 MeV that is associated with proton excitation into the $0g_{9/2}$ orbital. The yrast $9/2^-$ and $11/2^-$ levels observed in the lower-Z isotones are clearly identified at 1.572 and 2.165 MeV, respectively.

Excellent data are available for the levels of ^{86}Kr . The new beta-decay data from the 1^- ^{86}Br ground state leads directly to a certain 2^- assignment for the level at 4.316 MeV [57]. There is good agreement also for the high-spin levels from studies by two different groups [58], [59]. There are Coulex data for the 2^+ and 3^- levels and a surprising long 3-ns half-life for the 4_1^+ level.

Results of the p35-i3 SVD fit.

The first state for each nucleus gives the ground state energy in MeV. The other states for each nucleus are excitation energies in MeV. The table gives the experiment energy, the fitted energy and the energy difference.

Nucleus	2J	parity	exp	fitted	difference
1 Cu	79	5 -	-657.354	-657.437	-0.083
2 Cu	79	3 -	0.656	0.761	0.105
3 Cu	79	1 -	1.511	1.550	0.039
4 Zn	80	0 +	-673.884	-673.802	0.082
5 Zn	80	4 +	1.497	1.532	0.035
6 Zn	80	8 +	1.979	2.068	0.089
7 Zn	80	4 +	2.630	2.490	-0.140
8 Ga	81	5 -	-687.152	-687.104	0.048
9 Ga	81	3 -	0.351	0.397	0.046
10 Ga	81	3 -	0.803	0.615	-0.188
11 Ga	81	9 -	1.236	1.415	0.179
12 Ga	81	11 -	1.952	1.937	-0.015
13 Ge	82	0 +	-702.228	-702.046	0.182
14 Ge	82	4 +	1.348	1.591	0.243
15 Ge	82	4 +	2.216	2.332	0.116
16 Ge	82	8 +	2.288	2.169	-0.119
17 Ge	82	0 +	2.333	2.463	0.130
18 Ge	82	8 +	2.524	2.370	-0.154
19 Ge	82	6 +	2.702	2.702	-0.000
20 Ge	82	2 +	2.714	2.774	0.060
21 As	83	5 -	-713.771	-713.688	0.083
22 As	83	3 -	0.307	0.094	-0.213
23 As	83	3 -	0.712	0.977	0.265
24 As	83	1 -	1.194	1.152	-0.042
25 As	83	9 -	1.543	1.589	0.046
26 As	83	11 -	1.867	1.788	-0.079
27 Se	84	0 +	-727.339	-727.205	0.134
28 Se	84	4 +	1.454	1.781	0.327
29 Se	84	8 +	2.122	2.199	0.077
30 Se	84	4 +	2.461	2.457	-0.004
31 Se	84	0 +	1.967	1.776	-0.191
32 Se	84	6 +	2.700	2.523	-0.177
33 Br	85	3 -	-737.255	-737.367	-0.112
34 Br	85	5 -	0.345	0.425	0.080
35 Br	85	3 -	0.956	0.901	-0.055
36 Br	85	1 -	1.191	1.092	-0.099
37 Br	85	7 -	1.427	1.331	-0.096
38 Br	85	5 -	1.553	1.477	-0.076
39 Br	85	9 -	1.571	1.569	-0.002
40 Br	85	3 -	1.725	1.680	-0.045
41 Br	85	1 -	1.795	1.643	-0.152
42 Br	85	9 +	1.859	2.123	0.264
43 Br	85	11 -	2.165	2.071	-0.094
44 Br	85	15 +	3.856	3.961	0.105
45 Kr	86	0 +	-749.234	-749.299	-0.065
46 Kr	86	4 +	1.565	1.648	0.083
47 Kr	86	8 +	2.250	2.243	-0.007
48 Kr	86	4 +	2.349	2.438	0.089

49 Kr 86 6 +	2.917	3.051	0.134	105 Nb 91 3 -	1.613	1.568	-0.045
50 Kr 86 6 -	3.099	3.275	0.176	106 Nb 91 9 +	1.637	1.635	-0.002
51 Kr 86 10 -	3.935	3.858	-0.077	107 Nb 91 9 -	1.790	1.864	0.074
52 Kr 86 12 -	4.431	4.345	-0.086	108 Nb 91 13 -	1.984	2.001	0.017
53 Rb 87 3 -	-757.856	-757.953	-0.097	109 Nb 91 17 -	2.034	2.038	0.004
54 Rb 87 5 -	0.403	0.436	0.033	110 Nb 91 13 +	2.290	2.273	-0.017
55 Rb 87 1 -	0.845	0.687	-0.158	111 Nb 91 11 -	2.413	2.459	0.046
56 Rb 87 7 -	1.349	1.575	0.226	112 Nb 91 15 -	2.660	2.749	0.089
57 Rb 87 3 -	1.390	1.221	-0.169	113 Nb 91 17 +	3.110	3.148	0.038
58 Rb 87 1 -	1.463	1.399	-0.064	114 Nb 91 21 +	3.466	3.518	0.052
59 Rb 87 9 +	1.578	1.540	-0.038	115 Mo 92 0 +	-796.511	-796.471	0.040
60 Rb 87 5 -	1.678	1.898	0.220	116 Mo 92 4 +	1.510	1.560	0.050
61 Rb 87 11 +	3.001	3.050	0.049	117 Mo 92 8 +	2.283	2.296	0.013
62 Rb 87 13 +	3.099	3.082	-0.017	118 Mo 92 0 +	2.520	2.515	-0.005
63 Rb 87 15 +	3.644	3.523	-0.121	119 Mo 92 10 -	2.527	2.467	-0.060
64 Rb 87 17 +	4.151	4.065	-0.086	120 Mo 92 12 +	2.612	2.551	-0.061
65 Sr 88 0 +	-768.468	-768.531	-0.062	121 Mo 92 16 +	2.760	2.656	-0.104
66 Sr 88 4 +	1.836	1.848	0.012	122 Mo 92 6 -	2.850	2.893	0.043
67 Sr 88 6 -	2.734	2.649	-0.085	123 Tc 93 9 +	-800.598	-800.598	-0.000
68 Sr 88 0 +	3.156	3.227	0.071	124 Tc 93 1 -	0.392	0.382	-0.010
69 Sr 88 4 +	3.218	3.140	-0.078	125 Tc 93 7 +	0.681	0.758	0.077
70 Sr 88 6 +	3.635	3.495	-0.140	126 Tc 93 5 -	1.408	1.414	0.006
71 Sr 88 2 +	3.487	3.457	-0.030	127 Tc 93 13 +	1.434	1.473	0.039
72 Sr 88 10 -	3.585	3.519	-0.066	128 Tc 93 11 +	1.516	1.551	0.035
73 Sr 88 8 -	3.953	3.841	-0.112	129 Tc 93 13 -	2.185	2.172	-0.013
74 Sr 88 12 -	4.020	4.072	0.052	130 Tc 93 17 +	2.185	2.230	0.045
75 Y 89 1 -	-775.547	-775.622	-0.075	131 Tc 93 17 -	2.185	2.170	-0.015
76 Y 89 9 +	0.909	0.878	-0.031	132 Tc 93 21 +	2.535	2.521	-0.014
77 Y 89 3 -	1.507	1.531	0.024	133 Tc 93 21 -	3.281	3.291	0.010
78 Y 89 5 -	1.745	1.592	-0.153	134 Tc 93 25 -	3.888	3.965	0.077
79 Y 89 5 +	2.222	1.994	-0.228	135 Ru 94 0 +	-806.864	-806.781	0.083
80 Y 89 7 +	2.530	2.546	0.016	136 Ru 94 4 +	1.431	1.473	0.042
81 Y 89 11 +	2.567	2.499	-0.068	137 Ru 94 8 +	2.187	2.184	-0.003
82 Y 89 9 +	2.622	2.770	0.148	138 Ru 94 12 +	2.498	2.464	-0.034
83 Y 89 13 +	2.893	2.842	-0.051	139 Ru 94 8 +	2.503	2.472	-0.031
84 Y 89 13 -	3.343	3.231	-0.112	140 Ru 94 10 -	2.624	2.569	-0.055
85 Y 89 15 -	4.132	4.078	-0.054	141 Ru 94 16 +	2.644	2.551	-0.093
86 Y 89 17 -	4.450	4.450	-0.000	142 Ru 94 0 +	2.995	3.049	0.054
87 Y 89 19 -	4.839	4.973	0.134	143 Ru 94 14 -	3.658	3.607	-0.051
88 Zr 90 0 +	-783.897	-783.920	-0.023	144 Rh 95 9 +	-809.910	-809.879	0.031
89 Zr 90 0 +	1.761	1.760	-0.001	145 Rh 95 1 -	0.543	0.560	0.017
90 Zr 90 4 +	2.186	2.200	0.014	146 Rh 95 7 +	0.680	0.706	0.026
91 Zr 90 10 -	2.319	2.286	-0.033	147 Rh 95 5 +	1.180	1.232	0.052
92 Zr 90 8 -	2.739	2.695	-0.044	148 Rh 95 13 +	1.351	1.401	0.050
93 Zr 90 6 -	2.748	2.703	-0.045	149 Rh 95 11 +	1.430	1.479	0.049
94 Zr 90 8 +	3.077	3.071	-0.006	150 Rh 95 17 +	2.068	2.134	0.066
95 Zr 90 4 +	3.309	3.446	0.137	151 Rh 95 17 -	2.236	2.232	-0.004
96 Zr 90 12 +	3.448	3.402	-0.046	152 Rh 95 21 +	2.450	2.453	0.003
97 Zr 90 16 +	3.589	3.505	-0.084	153 Rh 95 21 -	3.243	3.289	0.046
98 Zr 90 18 +	5.248	5.170	-0.078	154 Rh 95 25 +	3.724	3.848	0.124
99 Zr 90 20 +	5.644	5.476	-0.168	155 Rh 95 25 -	3.909	3.954	0.045
100 Nb 91 9 +	-789.052	-789.117	-0.065	156 Pd 96 0 +	-815.042	-814.964	0.078
101 Nb 91 1 -	0.105	0.097	-0.008	157 Pd 96 4 +	1.415	1.412	-0.003
102 Nb 91 5 -	1.187	1.194	0.007	158 Pd 96 8 +	2.099	2.127	0.028
103 Nb 91 3 -	1.313	1.361	0.048	159 Pd 96 12 +	2.424	2.369	-0.055
104 Nb 91 7 +	1.581	1.558	-0.023	160 Pd 96 16 +	2.531	2.482	-0.049

161 Pd 96 10 -	2.649	2.615	-0.034	1 2 2 3 2	0.3862
162 Pd 96 14 +	3.184	3.180	-0.004	1 2 4 4 2	-0.6077
163 Pd 96 20 +	3.784	3.815	0.031	1 3 1 3 2	0.1329
164 Ag 97 9 +	-817.052	-817.063	-0.011	1 3 2 2 2	0.0384
165 Ag 97 7 +	0.716	0.694	-0.022	1 3 2 3 2	-0.4775
166 Ag 97 13 +	1.290	1.321	0.031	1 3 4 4 2	0.5542
167 Ag 97 11 +	1.418	1.512	0.094	1 4 1 4 2	0.0421
168 Ag 97 9 +	1.673	1.750	0.077	2 2 2 2 2	0.2882
169 Ag 97 15 +	2.020	2.082	0.062	2 2 2 3 2	-0.4163
170 Ag 97 17 +	2.053	2.124	0.071	2 2 4 4 2	0.6484
171 Ag 97 21 +	2.343	2.401	0.058	2 3 2 3 2	0.1423
172 Cd 98 0 +	-821.073	-821.087	-0.014	2 3 4 4 2	0.3348
173 Cd 98 4 +	1.395	1.371	-0.024	4 4 4 4 2	-0.1620
174 Cd 98 8 +	2.082	2.090	0.008	1 2 1 2 3	0.8950
175 Cd 98 12 +	2.280	2.281	0.001	1 2 1 3 3	-0.1740
176 Cd 98 16 +	2.428	2.430	0.002	1 3 1 3 3	1.1166
177 Cd 98 10 -	2.627	2.619	-0.008	1 4 1 4 3	0.2328
178 In 99 9 +	-822.155	-822.201	-0.046	1 4 2 4 3	0.1689
179 In 99 1 -	0.671	0.734	0.063	2 4 2 4 3	-0.2489
180 In 99 3 -	1.780	1.782	0.002	1 1 1 1 4	0.5909
181 In 99 5 -	3.580	3.585	0.005	1 1 1 2 4	-0.0808
182 Sn 00 0 +	-825.163	-825.190	-0.027	1 1 4 4 4	0.0712

The p35-i3 Hamiltonian

All numbers are in units of MeV. The orbitals are labeled by k with $k = 1$ for $0f_{5/2}$, $k = 2$ for $1p_{3/2}$, $k = 3$ for $1p_{1/2}$, and $k = 4$ for $0g_{9/2}$. $\text{SPE}(1) = -14.8729$, $\text{SPE}(2) = -14.1118$, $\text{SPE}(3) = -13.3233$, and $\text{SPE}(4) = -9.7056$. The table contains k_1, k_2, k_3, k_4, J and $\text{TBME}(k_1, k_2, k_3, k_4, J, T = 1)$.

1 1 1 1 0	-0.4231	1 2 1 2 4	0.2474
1 1 2 2 0	-0.9062	1 2 4 4 4	-0.6290
1 1 3 3 0	-0.9527	1 4 1 4 4	0.5752
1 1 4 4 0	1.7602	1 4 2 4 4	0.1236
2 2 2 2 0	0.0985	1 4 3 4 4	-0.1368
2 2 3 3 0	-0.6757	2 4 2 4 4	0.6199
2 2 4 4 0	1.2092	2 4 3 4 4	-0.1014
3 3 3 3 0	0.4232	3 4 3 4 4	0.6132
3 3 4 4 0	0.7347	4 4 4 4 4	0.2891
4 4 4 4 0	-0.7997	1 4 1 4 5	0.2415
1 2 1 2 1	0.7977	1 4 2 4 5	0.0179
1 2 2 3 1	-0.0102	1 4 3 4 5	-0.4179
2 3 2 3 1	0.7258	2 4 2 4 5	0.1877
1 1 1 1 2	0.4175	2 4 3 4 5	0.2897
1 1 1 2 2	-0.2325	3 4 3 4 5	0.1333
1 1 1 3 2	-0.4466	1 4 1 4 6	0.5584
1 1 2 2 2	-0.2462	1 4 2 4 6	0.4964
1 1 2 3 2	-0.3913	2 4 2 4 6	0.8076
1 1 4 4 2	0.3924	4 4 4 4 6	0.4062
1 2 1 2 2	0.8217	1 4 1 4 7	-0.3052
1 2 1 3 2	0.2397	4 4 4 4 8	0.5553
1 2 2 2 2	0.2777		

-
- [1] M. Hjorth-Jensen, T. T. S. Kuo and E. Osnes, *Phys. Rep.* **261**, 125 (1995).
- [2] Z. H. Sun, T. D. Morris, G. Hagen, G. R. Jansen, and T. Papenbrock, *Phys. Rev. C* **98**, 054320 (2018).
- [3] S. R. Stroberg, H. Hergert, S. K. Bogner, and J. D. Holt, *Annu. Rev. Nucl. Part. Sci.* 2019. **69**, 307 (2019).
- [4] B. A. Brown and W. A. Richter, *Phys. Rev. C* **74**, 034315 (2006).
- [5] A. Magilligan and B. A. Brown, *Phys. Rev. C* **101**, 064312 (2020).
- [6] M. Honma, T. Otsuka, B. A. Brown and T. Mizusaki, *Phys. Rev. C* **69**, 034335 (2004).
- [7] M. Honma, T. Otsuka, T. Mizusaki, and M. Hjorth-Jensen, *Phys. Rev. C* **80**, 064323 (2009).
- [8] S. Mukhopadhyay, B. P. Crider, B. A. Brown, S. F. Ashley, A. Chakraborty, A. Kumar, E. E. Peters, M. T. McEllistrem, F. M. Prados-Estevéz, and S. W. Yates, *Phys. Rev. C* **95**, 014327 (2017).
- [9] A. Arima, S. Cohen, R. D. Lawson, and M. H. MacFarlane, *Nucl. Phys.* **A108**, 94 (1968).
- [10] B. H. Wildenthal, *Prog. Part. Nucl. Phys.* **11**, 5 (1984).
- [11] X. Ji and B. H. Wildenthal, *Phys. Rev. C* **37**, 1256 (1988).
- [12] A. F. Lisetskiy, B. A. Brown, M. Horoi and H. Grawe, *Phys. Rev. C* **70**, 044314 (2004).
- [13] Q. Yuan and B. S. Hu, *Phys. Lett. B* **858**, 139018 (2024).
- [14] I. Talmi and I. Unna, *Nucl. Phys.* **19**, 225 (1960).
- [15] S. Cohen, R. D. Lawson, M. H. Macfarlane, and M. Soga, *Phys. Lett.* **10**, 195 (1964).
- [16] N. Auerbach and I. Talmi, *Nucl. Phys.* **64**, 458 (1965).
- [17] J. Vervier, *Nucl. Phys.* **75**, 17 (1966).
- [18] J. B. Ball, J. B. McGrory, and J. S. Larsen, *Phys. Lett.* **41B**, 581 (1972).
- [19] D. H. Gloeckner and F. J. D. Serduke, *Nucl. Phys.* **A220**, 4 (1973).
- [20] J. Blomqvist and L. Rysdrom, *Phys. Scr.* **31**, 31 (1985).
- [21] L. Olivier et al., *Phys. Rev. Lett.* **119**, 19201 (2017).
- [22] L. Nies et al., *Phys. Rev. Lett.* **131**, 022502 (2023).
- [23] V. Vaquero et al, *Phys. Rev. Lett.* **124**, 022501 (2020).
- [24] K. Hebeler, S. K. Bogner, R. J. Furnstahl, A. Nogga, and A. Schwenk *Phys. Rev. C* **83**, 031301(R) (2011)
- [25] B. C. He and S. R. Stroberg, *Phys. Rev. C* **110**, 044317 (2024).
- [26] R. Taniuchi et al., *Nature* **569**, 53 (2019).
- [27] J. Taprogge et al. *Eur. Phys. J. A* (2016) **52**: 347
- [28] National Nuclear Data Center
- [29] J. Van de Walle, *Phys. Rev. Lett.* **107**, 142501 (2007).
- [30] Y. Shiga et al., *Phys. Rev. C* **93**, 024320 (2016).
- [31] MCSM
- [32] M. L. Cortes et al., *Phys. Rev. C* **97**, 044315 (2018).
- [33] V. Pazyi et al., *Phys. Rev. C* **102**, 014329 (2020).
- [34] B. Cheal et al., *Phys. Rev. Lett.* **104**, 252502 (2010).
- [35] J. Dudouet et al., *Phys. Rev. C* **100**, 011301(R) (2019).
- [36] L. Olivier., Ph.D. thesis, University Paris-Saclay, (2017)
- [37] Guillaume Maquart, Physique Nucleaire Experimental, Universtite de Lyon, (2017).
- [38] M. F. Alshudifat et al., *Phys.Rev. C* **93**, 044325 (2016).
- [39] D. Verney et al., *Phys. Rev. C* **76**, 054312 (2007).
- [40] T. Rzaca-Urban, W. Urban, J. L. Durell, A. G. Smith, and I. Ahmad, *Phys. Rev. C* **76**, 027302 (2007).
- [41] K. Hwang, J. H. Hamilton, A. V. Ramayya, N. T. Brewer, Y. X. Luo, J. O. Rasmussen, and S. J. Zhu, *Phys. Rev. C* **84**, 024305 (2011).
- [42] M. P. Carpenter et al., Physics Division Annual Report 2006, Argonne National Labortory.
- [43] E. Sahin, G. de Angelis, G. Duchene, T. Faul, A. Gadeaa, A. F. Lisetskiy, D. Ackermann, A. Algora, S. Aydinhi, F. Azaiez et al., *Nucl. Phys. A* **893**, 1 (2012).
- [44] D. Wilmsen, Thesis, Universite de Caen Normandie (2017).
- [45] Thisse, D., Lebois, M., Verney, D. et al. *Eur. Phys. J. A* **59**, 153 (2023)
- [46] K. Sieja and F. Nowacki, *Phys. Rev. C* **85**, 051301(R) (2012).
- [47] A. Gade et al., *Phys. Rev. C* **81**, 064326 (2010).
- [48] P. Baczyk, W. Urban, D. Zlotowska, M. Czerwinski, T. Rzaca-Urban, A. Blanc, M. Jentschel, P. Mutti, U. Koster, T. Soldner, G. de France, G. Simpson, and C. A. Ur, *Phys. Rev. C* **91**, 047302 (2015)
- [49] K. Rezynkina et al., *Phys. Rev. C* **106**, 014320 (2022).
- [50] F. Drouet, G. S. Simpson, A. Vancraeynest, G. Gey, G. Kessedjian, T. Malkiewicz, M. Ramdhane, C. Sage, G. Thiamova, T. Grahn et al., *EPJ Web Conf.* **62**, 01005 (2013), DOI: 10.1051/epjconf/20136201005
- [51] M. G. Porquet et al., *Phys. Rev. C* **84**, 054305 (2011)
- [52] J. A. Winger, J. C. Hill, F. K. Wohn, R. L. Gill, X. Ji, and B.H. Wildenthal, *Phys. Rev. C* **38**, 285 (1988).
- [53] P. Hoff and B. Fogelberg, *Nucl. Phys. A* **368**, 210 (1981).
- [54] J. Litzenger et al., *Phys. Rev. C* **92**, 064322 (2015).
- [55] S. M. Mullins, D. L. Watson, H. T. Fortune, *Phys. Rev. C* **37**, 587 (1988).
- [56] J. D. Knight, C. J. Orth, W. T. Leland and A. B. Tucker, *Phys. Rev. C* **9**, 1467 (1974).
- [57] W. Urban et al., *Phys. Rev. C* **94**, 044328 (2016).
- [58] A. Prevost et al., *Eur. Phys. J A* **22**, 391 (2004).
- [59] G. Winter, L. Funke, R. Schwengner, H. Prade, R. Wirovski, N. Nicolay, A. Dewald, P. von Brentano, Z. *Phys. A* **343**, 369 (1992).